ACS NANO
Cite This: ACS Nano 2019, 13, 4677−4685
www.acsnano.org

ARTICLE

In Situ Study of Molecular Structure of Water and Ice Entrapped in Graphene Nanovessels

Seyed Mohammadreza Ghodsi,[†] Sushant Anand,[‡] Reza Shahbazian-Yassar,[‡] Tolou Shokuhfar,*[,†] and Constantine M. Megaridis*[,‡]

[†]Department of Bioengineering, University of Illinois at Chicago, Chicago, Illinois 60607, United States
[‡]Department of Mechanical and Industrial Engineering, University of Illinois at Chicago, Chicago, Illinois 60607, United States

Supporting Information

ABSTRACT: **Water is ubiquitous in natural systems, ranging from the vast oceans to the nanocapillaries in the earth crust or cellular organelles. In bulk or in intimate contact with solid surfaces, water molecules arrange themselves according to their hydrogen (H) bonding, which critically affects their short- and long-range molecular structures. Formation of H-bonds among water molecules designates the energy levels of certain nonbonding molecular orbitals of water, which are quantifiable by spectroscopic techniques. While the molecular architecture of water in nanoenclosures is of particular interest to both science and industry, it requires fine spectroscopic probes with nanometer spatial resolution and sub-eV energy sensitivity. Graphene liquid cells (GLCs), which feature opposing closely spaced sheets of hydrophobic graphene, facilitate high-resolution transmission electron microscopy (TEM) and electron energy-loss spectroscopy (EELS) measurements of attoliter water volumes encapsulated tightly in the GLC nanovessels. We perform *in situ* TEM and EELS analysis of water encased in thin GLCs exposed to room and cryogenic temperatures to examine the nanoscale arrangement of the contained water molecules. Simultaneous quantification of GLC thickness leads to the conclusion that H-bonding strengthens under increased water confinement. The present results demonstrate the feasibility of nanoscale chemical characterization of aqueous fluids trapped in GLC nanovessels and offer insights on water molecule arrangement under high-confinement conditions.**

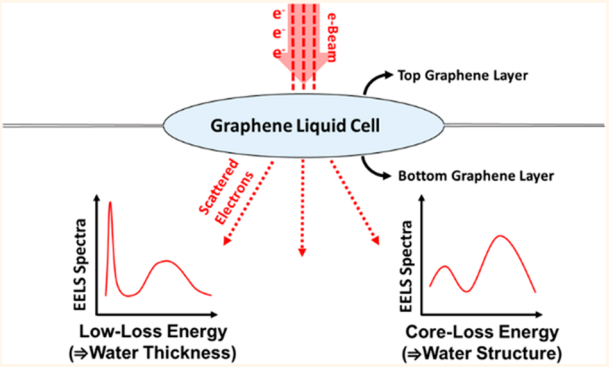

KEYWORDS: *nanoscale confinement, graphene, water, hydrogen bonding, TEM, EELS*

Understanding the behavior of water under various physical conditions has been of key interest because of its importance to life and nearly every human activity.[1] Electron affinity dissimilarities of oxygen and hydrogen cores cause a 1.8546 D permanent dipole on isolated water molecules. The bonding between the lone electron pair on the outermost orbital of an oxygen atom with polarized hydrogen atoms of neighboring water molecules gives rise to intermolecular forces, also known as, hydrogen bonding.[2] Although typical intermolecular energies in fluids exhibit magnitudes below 0.5 eV, hydrogen bonding between water molecules is substantial and may reach up to 1 eV/bond.[3] Such significant energetic interactions between water molecules derive its unusual and peculiar properties, such as elevated boiling and melting points, high surface tension, *etc.*[4] In order to form hydrogen bonds, a water molecule donates its hydrogen or deuterium (donor), while a neighboring water molecule accepts the proton on its oxygen core (acceptor), making each water molecule capable of forming a tetrahedral crystal with four symmetrical hydrogen bonds. The O−O distance of two isolated hydrogen-bonded water molecules under ambient conditions is 2.97 Å and decreases upon the addition of more molecules, converging to 2.76 Å in hexagonal ice.[5] However, the short lifetime of hydrogen bonds and their fast-paced dynamics in the absence of external forces[6] disturbs the perfect tetrahedral hydrogen bonding structures in liquid water, forming asymmetrical structures with less than four hydrogen bonds present.[7,8] Fourier transform infrared spectroscopy measurements have detected small portions of loose hydroxyl groups in liquid water,[9] indicating the engagement of most hydrogen protons in hydrogen bonds, while the rest are stretching freely. Molecular orbital models also predicted that the chance of nonperfect tetrahedral structure formation in water with fewer than four hydrogen bonds is far from

Received: January 31, 2019
Accepted: March 25, 2019
Published: March 25, 2019

DOI: 10.1021/acsnano.9b00914
ACS Nano 2019, 13, 4677−4685

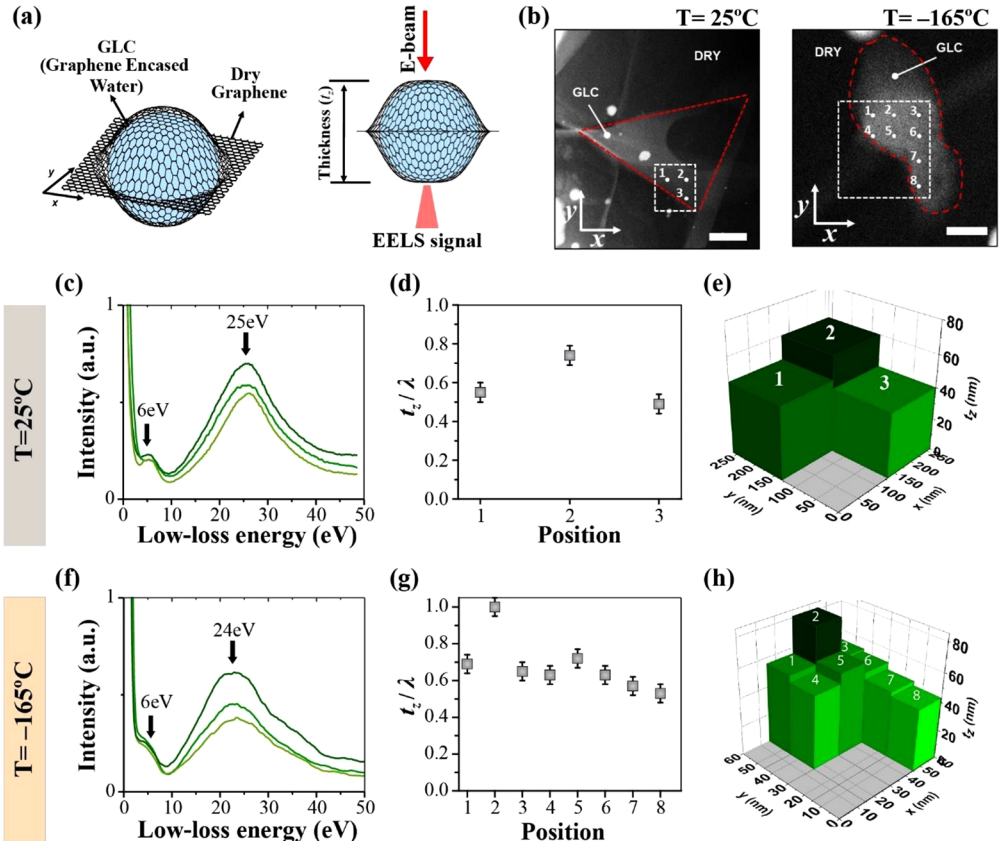

Figure 1. Analysis of low-loss EELS signals from graphene-encapsulated water. (a) High angle (left) and side view (right) schematic illustrations of a single GLC where an attoliter water volume is encased between opposing graphene layers. (b) STEM high angle annular dark field (HAADF) image of water encased in GLC at room temperature T = 25 °C (left) and at −165 °C (right). Water is tightly confined in each case inside the red-bounded domains. The white dash squares specify the sampling areas. Scale bars denote 300 (left) and 20 nm (right). (c) Low-loss EELS spectra showing features at 6−7 and 24 eV (plasmon peak), which have been previously reported for liquid water.[65] These low-loss spectra are used to measure the GLC sample thickness at different coordinates by correlating the log-ratio of inelastic mean free path of electrons in the sample. (d) $\frac{t_z}{\lambda}$ values of the GLC at 25 °C as estimated from the low-loss EELS spectrum in (c). (e) 3D bar graph of GLC nanovessel thickness derived from the data in (d). (f) Low-loss spectra of GLC-encased water at −165 °C show a slight shift of the plasmon peak toward lower energies. (g) $\frac{t_z}{\lambda}$ values of the GLC at −165 °C as estimated from the low-loss EELS spectrum in (f). (h) 3D bar graph of GLC nanovessel thickness derived from the data in (g).

negligible.[10] Following that, Pople claimed that bulk water possess a variety of molecular structures, including a four hydrogen-bonded one at any given temperature.[11] Such structural distortions are claimed to be the main reason behind the higher density of liquid water compared to that of ice, wherein symmetric tetrahedral H-bond structure population increases substantially.[1]

The architecture of water molecules closely confined between solid substrates has been a sought-after subject in science with numerous applications in the industry.[12] In many natural microscale environments, ranging from geology to biology, nanometer- to micrometer-thick films of water are bound in confined geometries enforced by solid surfaces.[13−15] A profound understanding of water behavior under such circumstances leads to industrial innovations in the field of nanofluidics.[16] Jones has described the behavior of water molecules entrapped between two nonpolar solid surfaces by simplifying the van der Waals (VdW) energy equation to $E_{\mathrm{VdW}} = \frac{A}{r_z^{12}} - \frac{C}{r_z^{6}}$, where A and C are positive coefficients, and r_z represents the confinement thickness.[17] When r_z approaches the water molecule radius (0.29 nm), E_{VdW} becomes dominant, and repulsion forces between surfaces and water molecules form structured bilayers of water close to the substrate.[18] Studying the behavior of water between two approaching hydrophilic mica spheres has shown oscillating repulsive forces with 0.25 nm periods, suggesting a certain degree of molecular layering in water upon close entrapment.[19] Potential energy landscape (PEL) simulations of entrapped water clusters between graphene crystals, a well-known nonpolar carbon layer with a hexagonal lattice structure, have predicted how enclosing water molecules between graphene substrates reorders the molecular arrangement of water.[20] In such simulations, water molecules exhibited highly ordered crystalline nuclei formation on the graphene layers with densities exceeding 1.2 g cm^{-3} at room temperature when wall spacings between graphene crystals fell below 1 nm.[20] Later on, atomic force microscopy (AFM) investigations showed the layer-by-layer growth of atomically flat water clusters between graphene crystals and BaF_2 substrates with height intervals of 0.37 nm, identical to the distance between adjacent bilayers in hexagonal ice.[21]

One hypothesis based on prior PEL simulations[20] and AFM observations[21−23] is that strong repulsive forces from close entrapment in graphene saturate hydrogen bonding in water

DOI: 10.1021/acsnano.9b00914
ACS Nano 2019, 13, 4677−4685

and preserve four-hydrogen-bonded structures of water molecules at room temperature. However, debate persists on the molecular structure of water trapped between solid surfaces. Although all proposed opinions are based on valid scientific assumptions and models,[24−26] they have often supported contradictory outcomes. This fundamental knowledge gap goes to the extent that some scientists believe hydrogen bonding dissociates upon capillary entrapment of water,[27,28] while others believe it is fortified instead.[26,29,30] Such challenges aside, development of spectroscopic tools have made it possible to probe the molecular structure and dynamics of water molecule behavior in significant detail. For example, examining the H-bonding moments of water in vapor, liquid, and solid states was made possible using environmental X-ray Raman spectroscopy (XRS).[31] XRS is capable of resolving the energy fluctuations in the outermost molecular orbital (MO) of water and distinguishes between single- and multihydrogen bonds between water molecules; thus, XRS has been used to assess the ratio of four-hydrogen-bonded species (symmetrical) to asymmetrical water structures.[11] Higher ratios of symmetrical to asymmetrical architecture indicate higher long-range tetrahedral arrangement of water molecules and thus, more solid-like behavior.[31,32] Despite the high-temporal resolution of X-ray Raman spectroscopy, the technique suffers from poor probe spot size (low spatial resolution) required for direct measurements of water in nano/micro capillaries.

Herein, we present a method to explore the behavior of water molecules under hydrophobic nanoscale entrapment (t_z ~ 50 nm). Using this data, we have also predicted the behavior of water molecules where the liquid thicknesses falls below 10 nm. The approach overcomes the challenges faced in previous works by combining visual (scanning transmission electron microscopy (STEM)) and spectroscopic (electron energy-loss spectroscopy (EELS)) methods to map the water-molecule arrangement with nanoscale resolution. Previous works have shown the potential of graphene liquid-cell (GLC) electron microscopy to study biological[33−35] and mineral[36−38] specimens under extreme confinement. We build on previous successes to entrap water between hydrophobic graphene sheets, which offer impermeable, yet flexible, substrates having negligible interactions with the water molecules.[39,40] EELS provides the opportunity to examine the film of water entrapped in graphene nanovessels using a fine (1 Å) electron probe with an energy resolution of 0.7 eV. While low-loss EELS specifies the vibrational and dielectric properties of the sample to measure the confinement thickness of water (which is important for establishing relations between molecular assembly and confinement), core-loss EELS examines the MO structure of water, which is correlated to the state of H-bonding between water molecules, providing insights on the arrangement of water molecules in nanoscale confinements. While the method is applied in graphene nanovessels, the approach can also be used to study other encased fluids whose spectra vary with spatial confinement.

RESULTS AND DISCUSSION

Depth Profiling of Water in Thin GLCs. In order to study the arrangement of water molecules encapsulated within GLC nanovessels, low-loss and core-loss EELS measurements were carried out at room and cryogenic temperatures to simultaneously analyze confinement thickness and MO fluctuations of the entrapped water phase. The reason for choosing room and cryogenic temperatures is that the specimen is most stable at these temperatures during imaging with the TEM cooling stage. Figure 1 illustrates how water gets encapsulated between two walls of graphene and presents the associated analysis of such volumes in the electron microscope. Specifically, Figure 1a depicts a GLC chamber (resembling a blister) from high angle (left) and at side view (right). A typical GLC with encapsulated water is comprised of regions that are filled with water, while other regions in the same vessel could be devoid of water (these constitute the dry region). This is exemplified in the STEM micrographs of Figure 1b, where separate GLCs are shown at room temperature (left) and cryogenic temperature (right). The numbered spots in Figure 1b (1, 2, and 3 in the sample at room temperature, and 1−8 on the cooled sample) mark the locations from where EELS spectra were acquired (e-beam target). The EELS collection area is as small as the electron beam cross section (~1 Å^2) with a local confinement thickness of t_z. The bubble on the top right corner of the GLC in Figure 1b (25 °C) was induced by a high current beam in the Ronchigram mode before the beam current was reduced in STEM mode to minimize water radiolysis. The presence of the liquid/gas interface separating the liquid (at left) from the bubble (right) confirms the successful entrapment of water between the graphene sheets.[41] The bright spots seen in Figure 1b (left) are copper residue, which remained on the graphene sheets from the etching process of the GLC fabrication (Figure S1).

The low-loss EELS signal (Figures 1c and S6) acquired at the designated numbered spots in Figure 1b for the sample at 25 °C shows the presence of a faint peak at 6−7 eV, followed by the plasmon peak at around 25 eV. Previous works have shown that these signals correspond to water, although the 6−7 eV has also been assigned to the graphene $\pi \rightarrow \pi^*$ plasmon.[42,43] The local thickness measurements of water GLC nanovessels were carried out using Egerton and Cheng's[44] EELS log-ratio technique (Figure 1d)

$$\frac{t_z}{\lambda} = \ln \frac{I_T}{I_0} \tag{1}$$

where λ is the characteristic inelastic mean free path of electrons in the sample, and the ratio $\frac{I_T}{I_0}$ is derived from the corresponding low-loss spectrum of Figure 1c. The value of λ in the GLC nanovessel is calculated from

$$\lambda = \frac{106FE_0}{E_M \ln \frac{2\beta E_0}{E_M}} \tag{2}$$

where E_0 is the electron acceleration energy in KeV, β is the electron detector collection semiangle (25 mrad), and F and E_M are functions of the sample atomic number (Z_{eff}).[44] For water in a GLC nanovessel, λ was estimated to be 80 nm at 80 keV. Using eq 1 in conjunction with eq 2, the thickness map of the water GLC nanovessels at T = 25 °C was obtained and is shown in Figure 1e. The thickness of the graphene layers (<1 nm) was considered negligible in comparison with the water film. The obtained profile of GLC nanovessels follows previously reported graphene geometry analysis, where GLC nanovessels over 100 nm in size exhibit near-octahedral geometry.[45] The low-loss EELS signal was also obtained at T = −165 °C using a different GLC sample. Similar to the 25 °C sample, we also obtained $\frac{t_z}{\lambda}$ values and the GLC thickness

DOI: 10.1021/acsnano.9b00914
ACS Nano 2019, 13, 4677−4685

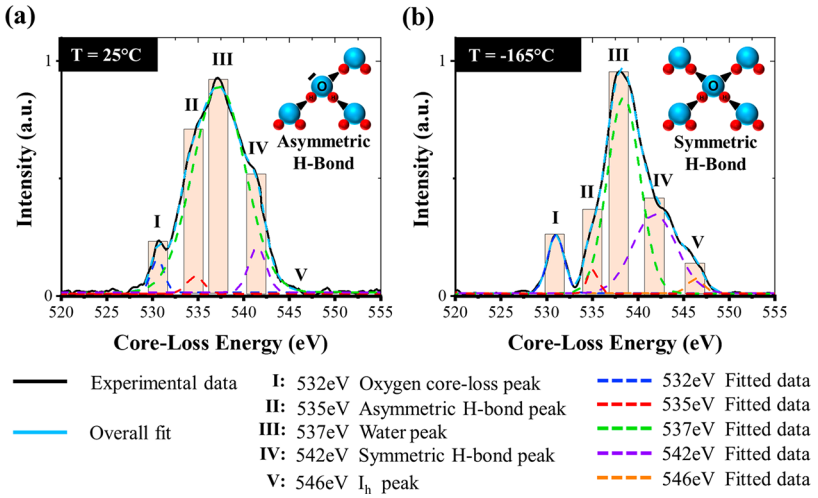

Figure 2. Oxygen core-loss spectra of water at 25 °C and −165 °C. (a) The oxygen core-loss of graphene-encapsulated water averaged over a sampling area at 25 °C shows peaks at 535 and 542 eV, which correspond, respectively, to $2b_2'$ and $2b_2''$ MOs of entrapped water. The strong $2b_2'$ peak compared to the $2b_2''$ peak at 25 °C shows the dominance of asymmetrical water structures in the body of water (inset). (b) The oxygen core-loss of graphene-entrapped water averaged over a sampling area at −165 °C. The accentuated peak at 542 eV, compared to the feature at 535 eV, represents highly populated four-hydrogen bonds in entrapped ice with near-perfect symmetry (schematically shown in the inset). The peak at 546 eV in water at −165 °C corresponds to hexagonal ice in the sample.

profile for the cooled sample (Figures 1f–h and S4). The plasmon peak position is a function of GLC nanovessel content as well as the vessel temperature; thus, the slight shift in the plasmon peak position from 25 to 24 eV at the cryogenic condition is expected.[46,47] While, EELS has shown promising results in measuring the thickness of samples with nanometer resolution,[46,48] future efforts can include the cross checking of thickness measurements with the AFM method.[49]

Probing H-Bonding of Water at Room and Cryogenic Temperatures. Next, to study how the arrangement of water molecules changes with temperature, core-loss EELS spectra of water at both room and cryogenic temperatures were acquired (core-loss peak of dry graphene can be found in Figure S3). Figure 2 illustrates such EELS spectra for GLC-trapped water at 25 (Figure 2a) and −165 °C (Figure 2b). The oxygen core-loss peaks were averaged over the sampling area (designated in Figure 1b). These EELS signal fluctuations are directly correlated to the state of the $2b_2$ orbital in water molecules and their hydrogen bonding architecture in GLC nanovessels.

Oxygen core-loss has a *K*-edge peak at 532 eV and near-edge structures at 535, 537, and 542 eV (associated with water molecules), which correspond to the promotion of the oxygen *K*-shell electrons, $1a_1$ (1s), to Rydberg orbitals.[31,50−52] More specifically, the 537 eV peak corresponds to the excitation of the oxygen 1s electron to the $2b_2$ orbital (2p) in a water molecule.[53,54] The peaks at 535 and 542 eV at 25 and −165 °C stem from intermolecular hydrogen bonding in the body of water. The split in the water oxygen core-loss to 535 and 542 eV has been previously reported in XRS experiments on liquid water at ambient condition (25 °C),[31,32,55] where hybridization of the 537 eV peak in water to a pre- and post-peak ($2b_2'$ and $2b_2''$, respectively) was unfolded. The latter peak ($2b_2''$) is dominant in ice (four-hydrogen bond structure), while the former peak ($2b_2'$) is accentuated in water molecules with less than four hydrogen bonds in place. Herein, the main EELS peak of water is located at 537 eV, while the pre-edge takes place at 535 eV (strong asymmetrical hydrogen bonding) and the post-edge at 542 eV (strong symmetrical hydrogen bonding). Some noise and signal overlaps observed in Figures 2 and S5 are inevitable results of specimen thickness which has reduced the EELS energy-resolution. Future studies can benefit from using ultrahigh energy resolution electron microscopes, such as monochromated TEMs, to improve the accuracy of the EELS results, enabling a fully energy-resolved and noise-free water signal.[47,56]

By comparing the near edge core-loss peaks of water at 25 °C in Figure 2a, the accentuated peak at 535 eV (compared to 542 eV) denotes the prominence of asymmetrical water molecular structures with fewer than four hydrogen bonds in place, although four-hydrogen-bonded structures are also present. Meanwhile, at −165 °C (Figure 2b), the intensity of the pre-peak at 535 eV has plunged, while the peaks at 537 and 542 eV have relatively intensified and broadened. The ratio of post-edge to pre-edge peaks in water at 25 to −165 °C has increased, indicating the enhanced hydrogen bonding in water upon reducing the temperature. Considering the super-hydrophobic nature of graphene,[22] we can safely neglect the hydrogen bonding between water molecules and the graphene membranes. The present results are in good agreement with previously reported neutron diffractometry measurements, where an enhancement in H-bonding was observed upon reducing the temperature.[8] The feature at 546 eV in Figure 2b represents the existence of ice in hexagonal form at −165 °C (the structure of water crystals are discussed further below).[57] While previous EELS measurements of entrapped thin water films (<1.0 nm) have shown a single oxygen peak at 542 eV (identical to our $2b_2''$ post-peak),[52] we report herein additional peaks in GLC-encased water, which stem from our relatively thicker samples ($t_z \sim 50$ nm).

Probing H-Bonding of Water under Confinement. The near edge core-loss EELS spectra of oxygen can fluctuate with temperature variations or graphene-cell thickness. While the effect of temperature on the molecular structure of water was examined by area-averaged EELS measurements in Figure 2, the contribution of GLC thickness on the population of four-hydrogen-bonded clusters at 25 and −165 °C was evaluated by recording the point EELS measurements of GLC nanovessels (each EELS collection point in Figure 3 has a

DOI: 10.1021/acsnano.9b00914
ACS Nano 2019, 13, 4677−4685

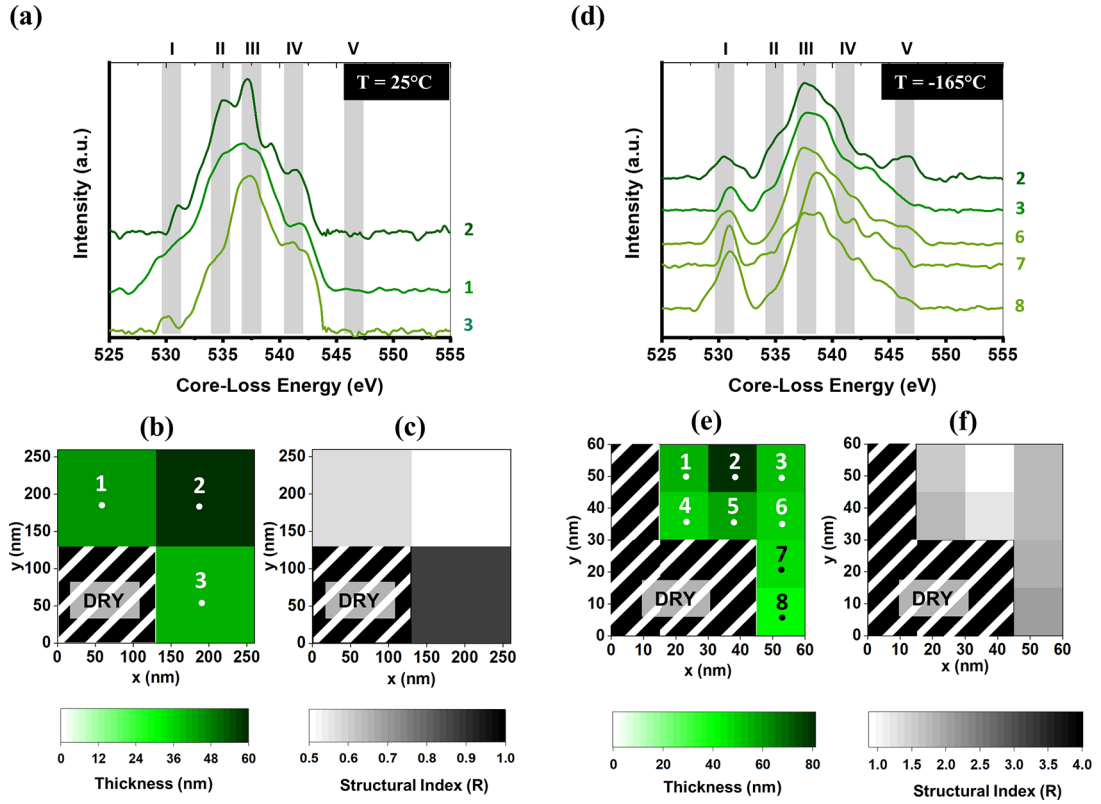

Figure 3. Oxygen core-loss spectra of water at designated spots. (a) Evolution of oxygen near-edge EELS spectra of water at 25 °C. (b) Map of sample thickness associated with each spot in the STEM-HAADF image of Figure 1b (left). (c) Map of structural index (R) at the three spots marked in Figure 1b (left); R increases toward the cell edges at rate of 0.02 nm^{-1} (diagonal lines cover the dry region, no data). (d) Evolution of oxygen near-edge EELS spectra of water cooled down to −165 °C. (e) Map of graphene cell thickness associated with each spot marked in the STEM-HAADF image of Figure 1b (right). (f) Structural index map showing R to increase toward the GLC nanovessel edges at a rate of 0.04 nm^{-1} (diagonal lines mark the dry region, no data).

cross-section area similar to Figure 1). Figure 3a depicts the EELS spectra derived from three points (marked in Figure 1b) at T = 25 °C. The map of local thickness of the GLC at these locations is shown in Figure 3b. An index to measure the water structure was derived from Egerton's equation[48] using the ratio of EELS intensity signals at 542 (I_{542}) and 535 eV (I_{535}). Following Egerton's approach, the number of atoms of element a per unit area in the sample is correlated to its EELS spectrum by

$$n_a = \frac{I_a}{I_{zlp}\sigma t} \tag{3}$$

where I_{zlp} is the zero-loss peak intensity, I_a is the peak intensity of element a, σ is the sample ionization cross-section, and t is the local sample thickness.[58] Thus, the ratio of hydrogen-bonds with different structures (n_{535} and n_{542}) can be derived by dividing the intensity of each peak (I_{535} and I_{542}), while I_{zlp} and σ stay unchanged. Thus, the ratio of four-hydrogen-bonded water structures to the asymmetrical hydrogen-bonded structures at a given temperature can be estimated by the structural index R

$$R = \frac{I_{542}}{I_{535}} \tag{4}$$

Figure 3c maps the derived R values with respect to the GLC coordinates at T = 25 °C. Figure 3d−f illustrates core-loss EEL spectra, respective thickness, and R values of water at T = −165 °C from the eight numbered locations marked in Figure 1b (the core-loss spectra of water at T = −165 °C can be found in Figure S5).

We now employ the maps of local cell thickness t_z and structural index R, as shown in Figure 3, to derive conclusions on how water molecules are organized inside the GLC cell. The higher values of R toward the GLC nanovessel edges indicate a higher four-hydrogen-bonded water population under relatively tighter wall spacings. The structural index oscillates around 0.5 for GLC nanovessels at room temperature (meaning that $n_{535} > n_{542}$), while R surpasses 1 and reaches up to 2.2 at cryogenic temperature (meaning that $n_{535} < n_{542}$). The thicknesses mapped in Figure 3b,e reaches down to 30 nm.

As is evident from Figure 3a, moving from a relatively thicker area (3D) in the direction of GLC edges coincides with an increased probability for four hydrogen-bonded water structures. Using the rate of change in the structural index R with respect to t_z at 25 °C (0.02 nm^{-1}), we find via extrapolation that R surpasses 1.0 at 25 °C when the distance between the two layers of graphene falls below 1 nm. This finding is important, as it indicates a certain degree of stratification in water well above melting temperatures and under severe entrapment. The higher molecular order of water upon close entrapment stems from the substantial VdW interaction inside GLC nanovessels with declining graphene membrane spacings (Figure S7).[59] Molecular dynamic (MD) simulations have indicated that water assumes a flat bilayer structure when closely confined (<1 nm) between atomically smooth hydrophobic substrates (such as graphene).[18,60] MD

DOI: 10.1021/acsnano.9b00914
ACS Nano 2019, 13, 4677−4685

simulations of water films with inhomogeneous thickness entrapped between a flat plate and a convex tip have also shown that upon applying pressure, the zones closer to the probing tip solidify prior to other zones, indicating the higher population of long-range four-hydrogen-bonded clusters under tight entrapment.[61] In either case, the structural index R is expected to soar by definition, as water molecules tend to form more compact structures via hydrogen bonding inside subnanometer confinements.

The same trend is observed for the encapsulated water at cryogenic conditions, where the structural index in the 3D regime increases with the spatial rate of 0.04 nm^{-1} in the direction of the edges (Figure 3b). Extrapolation of our data attained in the 3D regime shows that for a wall distance below 10 nm, asymmetrical hydrogen bonding structures diminish significantly. If this trend holds, when wall distance falls in the 1 nm regime, just four-hydrogen-bonded structures would survive at −165 °C. MD simulations confirm the instantaneous transformation of *quasi* 2D (Q2D) water to the energetically favored flat hexagonal ice bilayer upon decreasing temperatures (Nebraska ice).[18,60,62] The structural index R is expected to reach its maximum in such an H-bonding saturated bilayer ice.

The type of ice formed in graphene enclosures is also a matter of importance. The melting temperature of ice in the GLC system is well above −165 °C,[63] suggesting the existence of solid state water in our graphene nanoenclosure (as also established earlier based on the EELS data). The cooling rate of the system (around 5 °C/min) is slow enough so as to expect crystalline ice formation, according to Kobayashi *et al.*, who performed EELS measurements on ice I.[57] In 3D arrangement zones, where our EELS measurements take place, the competition among the growth axes (x, y, and z) results in a large concentration of stacking faults.[8] However, EELS is not capable of resolving the stacking faults nor the type of ice formed inside GLCs, except for ice I. EELS of water under cryogenic conditions has a distinct peak at 546 eV, which is attributed to hexagonal ice.[57] Density functional theory (DFT) calculations have predicted an identical EEL spectrum for two main polymorphs of ice I, namely hexagonal (I_h) and cubic ice (I_c), making them indistinguishable in EELS.[57] There are no prior EELS results on resolving other forms of ice. Although Figure 3b indicates the existence of hexagonal ice in water at −165 °C, it seems that the peak intensity for ice I at 546 eV does not correlate with the graphene membrane spacing (t_z). While a high population of ice I under cryogenic conditions and confinement thicknesses higher than 50 nm has been reported previously,[59] it is becoming more clear that ice I does not fit completely with either hexagonal or cubic ice but rather with a combination of both, with stacking faults (I_{sd}) that are not only a function of sample thickness but also of the freezing rate, local geometry of the nanoscale vessels, and also their surface chemistry.[64] The sample pressure also plays a significant role in the type of ice formed inside GLCs. While there are claims that the GLC sample contents are closer to the ambient pressure,[65] there is evidence supporting higher pressures inside GLCs upon water encapsulation.[52] While ice I is expected to exist under pressures up to 0.2 GPa and a temperature of −165 °C, increasing the pressure could shift the type of ice to transitional phases of ice II and III.[60] Unfortunately, current experimental tools are not sufficient to precisely identify the type of ice inside GLCs.

Radiolysis and its effects on water molecules are very important in liquid-cell TEM. The electron beam undergoes inelastic scattering events in water, resulting in the dissociation of a number of water molecules and the release of radicals (mostly hydroxyl groups).[66,67] While the content of the GLC is susceptible to radiolysis, reducing the electron beam current and the number of electron scattering events also minimizes the concentration of dissolved electrons and radicals in the fluid specimen and brings the nanoenvironment of GLC to equilibrium.[65] Under equilibrium conditions, the radiolysis byproducts recombine and neutralize the liquid environment, which, in turn, minimizes the complicating effects of radiolysis on the local structure of water molecules.[68] Herein, after identifying the subject GLC in the Ronchigram mode (high electron beam dose rate), STEM observations were performed with a 5 μA beam current and 40 μm objective aperture, which reduced the current even further. The electron beam dose rate during our EELS analysis was estimated to be around 0.3 e $Å^{-2}s^{-1}$ on the specimen, which is well below the intensity threshold of water dissociation (6−9 e $Å^{-2}s^{-1}$).[65,69] Moreover, the GLC thickness in the present tests was always below the inelastic mean free path of electrons in water (Figure 1), which keeps the average number of inelastic scattering events to 1. Figure S2 depicts a specimen after three successive EELS spot measurements. The stability of the liquid-free portion (bubble) in the GLC confirms the resilience of this sample in the low dose-rate electron beam condition and confirms our assertion that radiolysis did not play a significant role in the present tests.

CONCLUSIONS

While X-ray and neutron diffraction studies of bulk and pore water have shown the proper liquid/solid structures of water molecules and precisely measured the depression of water melting temperature under confinement,[50] these studies fall short in investigating the sample with nanoscale spatial resolution. AFM studies have proven phase transformation of entrapped water under severe confinement;[70] however, the conclusion was based on the precise thickness measurements of the water capsules without providing any insight on the water intermolecular structures. Herein, we have presented an *in situ* approach to analyze the intermolecular hydrogen bonding structure of nanoconfined water at different temperatures and confinement states. Such characterization requires the finest spectroscopic probe possible to precisely scan across the wet sample, without breaking the vacuum. This is not feasible using X-ray (large probe size) or traditional high-vacuum electron microscopy and spectroscopy techniques. Applying electron microscopy and spectroscopy on graphene-encapsulated water, we have measured the confinement thickness of water across the sample. A structural index of water at room and cryogenic temperatures was derived from the spectroscopic data, and was used to designate the prevalence of hydrogen bonding across the sample. The effect of temperature on the molecular architecture of graphene-entrapped water was studied by comparing the oxygen signals. The structural index of water at room temperature stayed below 1 in 3D regimes, while it exceeded 1 at subfreezing temperatures, indicating increased hydrogen-bonding density in water at lower temperatures. The effect of wall spacing on the molecular structure of confined water was studied by comparing the oxygen peaks at multiple locations on the sample, each having distinct confinement thickness, while

DOI: 10.1021/acsnano.9b00914
ACS Nano 2019, 13, 4677−4685

keeping the temperature constant. It was observed that the structural index of water rose with declining membrane wall separation (*i.e.*, higher confinement), suggesting the enhancement of intermolecular hydrogen bonding density in water under severe entrapment conditions. Our findings confirm the substantial role of confined geometries on the arrangement of water molecules.

METHODS/EXPERIMENTAL

Graphene crystals were grown using previously developed protocols based on the low pressure chemical vapor deposition (LPCVD) method.[71] Copper was annealed inside the LPCVD tube for 30 min prior to graphene growth. Subsequently, hydrogen and methane gases were allowed to flow in the tube with flow-rates of 7.0 and 5.0 SCCM, respectively, at 1000 °C. Graphene was grown on the copper substrate and transferred to TEM grids after etching and washing steps (direct graphene transfer method) (Figure S1).[69] The graphene/copper substrate was kept afloat on ammonium persulfate (APS) solution for 3 h to etch away the copper layer. The free-floating graphene layer was then carefully transferred with a microscope slide to DI water to wash off the etchant residue. The graphene layer was scooped by a 2000-mesh TEM grid, thus forming graphene-coated grids. APS and biological-grade DI water were purchased from Sigma-Aldrich. After deposition of DI water on the graphene side of the TEM grid, a second graphene layer was applied to seal water pockets between the graphene-coated grid and the overlaying layer of graphene. The grid was left in a desiccator overnight to evaporate excess amounts of water and form secure GLC nanovessels on the TEM grid. The grids were examined by TEM to make sure no salt residues were present. The ice phase of graphene-entrapped water was created by bringing the samples to liquid nitrogen temperature (−165 °C) inside the microscope using the Gatan cold stage holder. Once in the microscope, the temperature of GLC nanovessels was precisely monitored and manipulated through the Gatan cold-stage controller.

STEM of samples at the two temperatures (25 and −165 °C) was carried out in the aberration-corrected JEOL ARM-200F microscope operating at 80 keV with a beam current of 5 μA. Analytical EELS measurements on water GLCs were carried out using Gatan Quantum GIF with channel intervals of 0.15 eV. Low-loss and oxygen core-loss of GLC nanovessels with various thicknesses were acquired at the two temperatures. The beam flux on the sample was estimated to be 0.3 e $Å^{-2}s^{-1}$, which is well below the water dissociation threshold.[65] The thickness of GLC nanovessels was measured using the Egerton and Cheng correlation for EELS low-loss peak intensity analysis.[42,44] The geometry of GLC nanovessels was then reproduced using acquired thickness data, with the assumption of geometric symmetry over the lateral (x−y) plane, the OriginPro software suite, and Random Thin Plate Spline interpolation over the acquired data. The core-loss signal was processed with the Gatan Microscopy suite, and the background signal of the core-loss spectrum was removed using the $I = AE^{-r}$ law for all acquired data. The low-loss and oxygen core-loss signals were fitted with Gaussian curves to estimate the position of each peak.

ASSOCIATED CONTENT

Supporting Information

The Supporting Information is available free of charge on the ACS Publications website at DOI: 10.1021/acsnano.9b00914.

Details on GLC fabrication, beam heating, mitigating radiolysis defect in GLC, oxygen core-loss electron energy-loss spectroscopy of dry and wet graphene cells, low-loss EELS of water GLC, core-loss EELS of water GLC, core-loss EELS curve fitting, EELS energy resolution, and entropy of Q2D vs 3D regime (PDF)

AUTHOR INFORMATION

Corresponding Authors

*E-mail: tolou@uic.edu.
*E-mail: cmm@uic.edu.

ORCID

Seyed Mohammadreza Ghodsi: 0000-0002-7546-1253
Sushant Anand: 0000-0002-1480-1840
Reza Shahbazian-Yassar: 0000-0002-7744-4780
Constantine M. Megaridis: 0000-0002-6339-6933

Notes

The authors declare no competing financial interest.

ACKNOWLEDGMENTS

This material is based upon work supported by the National Science Foundation (NSF) under award 1805753. T. Shokuhfar was supported by NSF CAREER award 1564950. R. Shahbazian-Yassar acknowledges the financial support from NSF via award 1710049. The work made use of instruments in the Electron Microscopy Service of the Research Resources Center at UIC. The authors would like to thank V. Kulkarni for his assistance with the figures.

REFERENCES

(1) Brini, E.; Fennell, C. J.; Fernandez-Serra, M.; Hribar-Lee, B.; Lukšič, M.; Dill, K. A. How Water's Properties are Encoded in its Molecular Structure and Energies. *Chem. Rev.* **2017**, *117*, 12385−12414.

(2) Latimer, W. M.; Rodebush, W. H. Polarity and Ionization From the Standpoint of the Lewis Theory of Valence. *J. Am. Chem. Soc.* **1920**, *42*, 1419−1433.

(3) Marechal, Y. *The Hydrogen Bond and the Water Molecule*;-Aqueous and Bio-Media: Grenoble, 2006; pp 3−23.

(4) Shibata, S.; Bartell, L. S. Electron-Diffraction Study of Water and Heavy Water. *J. Chem. Phys.* **1965**, *42*, 1147−1151.

(5) Dyke, T. R.; Mack, K. M.; Muenter, J. S. The Structure of Water Dimer from Molecular Beam Electric Resonance Spectroscopy. *J. Chem. Phys.* **1977**, *66*, 498−510.

(6) Woutersen, S.; Mu, Y.; Stock, G.; Hamm, P. Hydrogen-Bond Lifetime Measured by Time-Resolved 2D-IR Spectroscopy: N-Methylacetamide in Methanol. *Chem. Phys.* **2001**, *266*, 137−147.

(7) Pettersson, L. G. M.; Nilsson, A. The Structure of Water; from Ambient to Deeply Supercooled. *J. Non-Cryst. Solids* **2015**, *407*, 399−417.

(8) Findenegg, G. H.; Jähnert, S.; Akcakayiran, D.; Schreiber, A. Freezing and Melting of Water Confined in Silica Nanopores. *ChemPhysChem* **2008**, *9*, 2651−2659.

(9) Wu, Y.; Mayer, J. T.; Garfunkel, E.; Madey, T. E. X-Ray Photoelectron Spectroscopy Study of Water Adsorption on BaF2(111) and CaF2(111) Surfaces. *Langmuir* **1994**, *10*, 1482−1487.

(10) Conde, M. M.; Vega, C.; Patrykiejew, A. The Thickness of a Liquid Layer on the Free Surface of Ice as Obtained from Computer Simulation. *J. Chem. Phys.* **2008**, *129*, 014702.

(11) Pople, J. A. Molecular Association in Liquids II. A Theory of the Structure of Water. *Proc. R. Soc. London A* **1951**, *205*, 163−178.

(12) Abgrall, P.; Nguyen, N. T. Nanofluidic Devices and Their Applications. *Anal. Chem.* **2008**, *80*, 2326−2341.

(13) Audette, G. F.; van Schaik, E. J.; Hazes, B.; Irvin, R. T. DNA-Binding Protein Nanotubes: Learning from Nature's Nanotech Examples. *Nano Lett.* **2004**, *4*, 1897−1902.

(14) Gravelle, S.; Joly, L.; Detcheverry, F.; Ybert, C.; Cottin-Bizonne, C.; Bocquet, L. Optimizing Water Permeability Through the Hourglass Shape of Aquaporins. *Proc. Natl. Acad. Sci. U. S. A.* **2013**, *110*, 16367−16372.

DOI: 10.1021/acsnano.9b00914
ACS Nano 2019, 13, 4677−4685

(15) Rasaiah, J. C.; Garde, S.; Hummer, G. Water in Nonpolar Confinement: From Nanotubes to Proteins and Beyond. *Annu. Rev. Phys. Chem.* **2008**, *59*, 713−740.
(16) Whitesides, G. M. What Comes Next? *Lab Chip* **2011**, *11*, 191−193.
(17) Jones, J. E. E. On the Determination of Molecular Fields. From Crystal Measurements and Kinetic Theory Data. *Proc. R. Soc. London, Ser. A* **1924**, *106*, 709−718.
(18) Koga, K.; Tanaka, H.; Zeng, X. C. First-Order Transition in Confined Water Between High-Density Liquid and Low-Density Amorphous Phases. *Nature* **2000**, *408*, 564.
(19) Israelachvili, J. N.; Pashley, R. M. Molecular Layering of Water at Surfaces and Origin of Repulsive Hydration Forces. *Nature* **1983**, *306*, 249−250.
(20) Lombardo, T. G.; Giovambattista, N.; Debenedetti, P. G. Structural and Mechanical Properties of Glassy Water in Nanoscale Confinement. *Faraday Discuss.* **2009**, *141*, 359−376.
(21) Verdaguer, A.; Segura, J. J.; Lopez-Mir, L.; Sauthier, G.; Fraxedas, J. (2013). Communication: Growing Room Temperature Ice with Graphene. *J. Chem. Phys.* **2013**, *138*, 121101.
(22) Cao, P.; Xu, K.; Varghese, J. O.; Heath, J. R. The Microscopic Structure of Adsorbed Water on Hydrophobic Surfaces Under Ambient Conditions. *Nano Lett.* **2011**, *11*, 5581−5586.
(23) Komurasaki, H.; Tsukamoto, T.; Yamazaki, K.; Ogino, T. Layered Structures of Interfacial Water and Their Effects on Raman Spectra in Graphene-on-Sapphire Systems. *J. Phys. Chem. C* **2012**, *116*, 10084−10089.
(24) Sotthewes, K.; Bampoulis, P.; Zandvliet, H. J. W.; Lohse, D.; Poelsema, B. Pressure-Induced Melting of Confined Ice. *ACS Nano* **2017**, *11*, 12723−12731.
(25) Zhao, W. H.; Wang, L.; Bai, J.; Yuan, L. F.; Yang, J.; Zeng, X. C. Highly Confined Water: Two-Dimensional Ice, Amorphous Ice, and Clathrate Hydrates. *Acc. Chem. Res.* **2014**, *47*, 2505−2513.
(26) Naguib, N.; Ye, H.; Gogotsi, Y.; Yazicioglu, A. G.; Megaridis, C. M.; Yoshimura, M. Observation of Water Confined in Nanometer Channels of Closed Carbon Nanotubes. *Nano Lett.* **2004**, *4*, 2237−2243.
(27) Gordillo, M. C.; Martı, J. Hydrogen Bond Structure of Liquid Water Confined in Nanotubes. *Chem. Phys. Lett.* **2000**, *329*, 341−345.
(28) Scatena, L. F.; Brown, M. G.; Richmond, G. L. Water at Hydrophobic Surfaces: Weak Hydrogen Bonding and Strong Orientation Effects. *Science* **2001**, *292*, 908−912.
(29) Di Leo, J. M.; Maranon. Confined Water in Nanotube. *J. Mol. Struct.: THEOCHEM* **2003**, *623*, 159−166.
(30) Hummer, G.; Rasaiah, J. C.; Noworyta, J. P. Water Conduction Through the Hydrophobic Channel of a Carbon Nanotube. *Nature* **2001**, *414*, 188.
(31) Myneni, S.; Luo, Y.; Näslund, L. Å.; Cavalleri, M.; Ojamäe, L.; Ogasawara, H.; Hussain, Z.; et al. Spectroscopic Probing of Local Hydrogen-Bonding Structures in Liquid Water. *J. Phys.: Condens. Matter* **2002**, *14*, L213−L219.
(32) Huang, C.; Wikfeldt, K. T.; Tokushima, T.; Nordlund, D.; Harada, Y.; Bergmann, U.; Ljungberg, M. P.; et al. The Inhomogeneous Structure of Water at Ambient Conditions. *Proc. Natl. Acad. Sci. U. S. A.* **2009**, *106*, 15214−15218.
(33) Ribeiro, A. R.; Mukherjee, A.; Hu, X.; Shafien, S.; Ghodsi, R.; He, K.; Gemini-Piperni, S.; Wang, C.; Klie, R. F.; Shokuhfar, T.; Shahbazian-Yassar, R.; et al. Bio-Camouflage of Anatase Nanoparticles Explored by *In Situ* High-Resolution Electron Microscopy. *Nanoscale* **2017**, *9*, 10684−10693.
(34) Park, J.; Park, H.; Ercius, P.; Pegoraro, A. F.; Xu, C.; Kim, J. W.; Han, S. H.; Weitz, D. A. Direct Observation of Wet Biological Samples by Graphene Liquid Cell Transmission Electron Microscopy. *Nano Lett.* **2015**, *15*, 4737−4744.
(35) Chen, Q.; Smith, J. M.; Park, J.; Kim, K.; Ho, D.; Rasool, H. I.; Zettl, A.; Alivisatos, A. P. 3D Motion of DNA-Au Nanoconjugates in Graphene Liquid Cell Electron Microscopy. *Nano Lett.* **2013**, *13*, 4556−61.
(36) Cheong, J. Y.; Chang, J. H.; Seo, H. K.; Yuk, J. M.; Shin, J. W.; Lee, J. Y.; Kim, I. D. Growth Dynamics of Solid Electrolyte Interphase Layer on SnO2 Nanotubes Realized by Graphene Liquid Cell Electron Microscopy. *Nano Energy* **2016**, *25*, 154−160.
(37) De Clercq, A.; Dachraoui, W.; Margeat, O.; Pelzer, K.; Henry, C. R.; Giorgio, S. Growth of Pt-Pd Nanoparticles Studied *In Situ* by HRTEM in a Liquid Cell. *J. Phys. Chem. Lett.* **2014**, *5*, 2126−2130.
(38) Ghodsi, S. M.; Megaridis, C. M.; Shahbazian-Yassar, R.; Shokuhfar, T. Advances in Graphene-Based Liquid Cell Electron Microscopy: Working Principles, Opportunities, and Challenges. *Small Methods* **2019**, 1900026.
(39) Berry, V. Impermeability of Graphene and its Applications. *Carbon* **2013**, *62*, 1−10.
(40) He, K.; Nie, A.; Yuan, Y.; Ghodsi, S. M.; Song, B.; Firlar, E.; Lu, J.; Lu, Y. P.; Shokuhfar, T.; Megaridis, C. M.; Shahbazian-Yassar, R. *In Situ* Transmission Electron Microscopy Explores a New Nanoscale Pathway for Direct Gypsum Formation in Aqueous Solution. *ACS Appl. Nano Mater.* **2018**, *1*, 5430−5440.
(41) Grogan, J. M.; Schneider, N. M.; Ross, F. M.; Bau, H. H. Bubble and Pattern Formation in Liquid Induced by an Electron Beam. *Nano Lett.* **2014**, *14*, 359−364.
(42) Holtz, M. E.; Yu, Y.; Gao, J.; Abruña, H. D.; Muller, D. A. *In situ* Electron Energy-Loss Spectroscopy in Liquids. *Microsc. Microanal.* **2013**, *19*, 1027−35.
(43) Soto, G. Electron Spectroscopic Identification of Carbon Species on CNx Films. *Mater. Lett.* **2001**, *49*, 352−356.
(44) Egerton, R. F.; Cheng, S. C. Measurement of Local Thickness by Electron Energy-Loss Spectroscopy. *Ultramicroscopy* **1987**, *21*, 231−244.
(45) Khestanova, E.; Guinea, F.; Fumagalli, L.; Geim, A. K.; Grigorieva, I. V. Universal Shape and Pressure Inside Bubbles Appearing in Van der Waals Heterostructures. *Nat. Commun.* **2016**, *7*, 12587.
(46) Hu, X.; Yasaei, P.; Jokisaari, J.; Öğüt, S.; Salehi-Khojin, A.; Klie, R. F. Mapping Thermal Expansion Coefficients in Freestanding 2D Materials at the Nanometer Scale. *Phys. Rev. Lett.* **2018**, *120*, 55902.
(47) Egerton, R. F. *Electron Energy-Loss Spectroscopy in the Electron Microscope*; Springer Science & Business Media: New York, 2011; pp 231−288.
(48) Malis, T.; Cheng, S. C.; Egerton, R. F. EELS Log-Ratio Technique for Specimen Thickness Measurement in the TEM. *J. Electron Microsc. Tech.* **1988**, *8*, 193−200.
(49) Nappini, S.; Matruglio, A.; Naumenko, D.; Dal Zilio, S.; Bondino, F.; Lazzarino, M.; Magnano, E. Graphene Nanobubbles on TiO2 for *In-Operando* Electron Spectroscopy of Liquid-Phase Chemistry. *Nanoscale* **2017**, *9*, 4456−4466.
(50) Näslund, L.Å.; Edwards, D. C.; Wernet, P.; Bergmann, U.; Ogasawara, H.; Pettersson, L. G.; Myneni, S.; Nilsson, A. X-Ray Absorption Spectroscopy Study of the Hydrogen Bond Network in the Bulk Water of Aqueous Solutions. *J. Phys. Chem. A* **2005**, *109*, 5995−6002.
(51) Wight, G. R.; Brion, C. E. K-Shell Excitation of CH4, NH3, H2O, CH3OH, CH3OCH3 and CH3NH2 by 2.5 keV Electron Impact. *J. Electron Spectrosc. Relat. Phenom.* **1974**, *3*, 191.
(52) Algara-Siller, G.; Lehtinen, O.; Wang, F. C.; Nair, R. R.; Kaiser, U.; Wu, H. A.; Geim, A. K.; Grigorieva, I. V. Square Ice in Graphene Nanocapillaries. *Nature* **2015**, *519*, 443−5.
(53) Jungjohann, K. L.; Evans, J. E.; Aguiar, J. A.; Arslan, I.; Browning, N. D. Atomic-Scale Imaging and Spectroscopy for *In Situ* Liquid Scanning Transmission Electron Microscopy. *Microsc. Microanal.* **2012**, *18*, 621−627.
(54) Guo, J.; Luo, Y. Molecular Structure in Water and Solutions Studied by Photon-In/Photon-Out Soft X-Ray Spectroscopy. *J. Electron Spectrosc. Relat. Phenom.* **2010**, *177*, 181−191.
(55) Smith, J. D.; Cappa, C. D.; Wilson, K. R.; Messer, B. M.; Cohen, R. C.; Saykally, R. J. Energetics of Hydrogen Bond Network Rearrangements in Liquid Water. *Science* **2004**, *306*, 851−853.
(56) Park, J.; Heo, S.; Chung, J. G.; Kim, H.; Lee, H.; Kim, K.; Park, G. S. Bandgap Measurement of Thin Dielectric Films Using

DOI: 10.1021/acsnano.9b00914
ACS Nano 2019, 13, 4677−4685

Monochromated STEM-EELS. *Ultramicroscopy* **2009**, *109*, 1183–1188.
(57) Kobayashi, K.; Koshino, M.; Suenaga, K. Atomically Resolved Images of Ih Ice Single Crystals in the Solid Phase. *Phys. Rev. Lett.* **2011**, *106*, 18–21.
(58) Hofer, F.; Kothleitner, G. Quantitative Microanalysis Using Electron Energy-Loss Spectrometry. I. Li and Be in Oxides. *Microsc., Microanal., Microstruct.* **1993**, *4*, 539–560.
(59) Cardellach, M.; Verdaguer, A.; Santiso, J.; Fraxedas, J. Two-Dimensional Wetting: The Role of Atomic Steps on the Nucleation of Thin Water Films on BaF2 (111) at Ambient Conditions. *J. Chem. Phys.* **2010**, *132*, 234708.
(60) Lupi, L.; Kastelowitz, N.; Molinero, V. Vapor Deposition of Water on Graphitic Surfaces: Formation of Amorphous Ice, Bilayer Ice, Ice I, and Liquid Water. *J. Chem. Phys.* **2014**, *141*, 18C508.
(61) Qiu, H.; Zeng, X. C.; Guo, W. Water in Inhomogeneous Nanoconfinement: Coexistence of Multilayered Liquid and Transition to Ice Nanoribbons. *ACS Nano* **2015**, *9*, 9877–9884.
(62) Kastelowitz, N.; Molinero, V. Ice–Liquid Oscillations in Nanoconfined Water. *ACS Nano* **2018**, *12*, 8234–8239.
(63) Christenson, H. K. Confinement Effects on Freezing and Melting. *J. Phys.: Condens. Matter* **2001**, *13*, R95.
(64) Malkin, T. L.; Murray, B. J.; Salzmann, C. G.; Molinero, V.; Pickering, S. J.; Whale, T. F. Stacking Disorder in Ice I. *Phys. Chem. Chem. Phys.* **2015**, *17*, 60–76.
(65) Wang, C.; Shokuhfar, T.; Klie, R. F. Precise *In Situ* Modulation of Local Liquid Chemistry *via* Electron Irradiation in Nanoreactors Based on Graphene Liquid Cells. *Adv. Mater.* **2016**, *28*, 7716–7722.
(66) Schneider, N. M.; Norton, M. M.; Mendel, B. J.; Grogan, J. M.; Ross, F. M.; Bau, H. H. Electron-Water Interactions and Implications for Liquid Cell Electron Microscopy. *J. Phys. Chem. C* **2014**, *118*, 22373–22382.
(67) Hill, M. A.; Smith, F. A. Calculation of Initial and Primary Yields in the Radiolysis of Water. *Radiat. Phys. Chem.* **1994**, *43*, 265–280.
(68) LaVerne, J. A.; Pimblott, S. M. Scavenger and Time Dependences of Radicals and Molecular Products in the Electron Radiolysis of Water: Examination of Experiments and Models. *J. Phys. Chem.* **1991**, *95*, 3196–3206.
(69) Wang, C.; Qiao, Q.; Shokuhfar, T.; Klie, R. F. High-Resolution Electron Microscopy and Spectroscopy of Ferritin in Biocompatible Graphene Liquid Cells and Graphene Sandwiches. *Adv. Mater.* **2014**, *26*, 3410–3414.
(70) Xu, K.; Cao, P.; Heath, J. R. Graphene Visualizes the First Water Adlayers on Mica at Ambient Conditions. *Science* **2010**, *329*, 1188–1191.
(71) Suk, J. W.; Kitt, A.; Magnuson, C. W.; Hao, Y.; Ahmed, S.; An, J.; Swan, A. K.; Goldberg, B. B.; Ruoff, R. S. Transfer of CVD-Grown Monolayer Graphene onto Arbitrary Substrates. *ACS Nano* **2011**, *5*, 6916–6924.

DOI: 10.1021/acsnano.9b00914
ACS Nano 2019, 13, 4677–4685